ChemComm

Synthesis and characterization of plasmonic peptoid nanosheets

Journal:	*ChemComm*
Manuscript ID	CC-COM-01-2021-000092.R1
Article Type:	Communication

COMMUNICATION

Synthesis and characterization of plasmonic peptoid nanosheets

Ellen J. Robertson,*[a] Chris Avanessian,[a†] Jana R. Davis,[a†] Anna K. Mahony,[a†] and Elizabeth V. Whitney[a†]

Received 00th January 20xx,
Accepted 00th January 20xx

DOI: 10.1039/x0xx00000x

Solvated two-dimensional (2D) arrays of gold nanoparticles (AuNPs) are versatile plasmonic materials that are not limited by the constraints of a solid support. We report here the assembly of AuNP-embedded peptoid nanosheets via monolayer collapse at the liquid-liquid interface. This synthesis route produces a new class of solvated 2D plasmonic arrays and has the potential to be extended to a variety of different nanoparticle systems.

Two dimensional (2D) arrays composed of plasmonic nanoparticles (NPs) are extensively used in a variety of technologies due to their interesting opto-electronic properties[1,2]. These arrays exhibit localized surface plasmon resonances (LSPRs) that result from light-induced oscillations of the conduction electrons of the NPs. LSPRs of individual plasmonic NPs are capable of coupling when they are arranged in close proximity[3]. When light is incident on a 2D plasmonic NP array that is resonant with the LSPR, an enhanced electromagnetic field is generated that is localized between adjacent NPs[1]. This effect of LSPR coupling makes 2D plasmonic NP arrays ideal components in sensing devices, such as those aimed at detecting harmful environmental contaminants using surface enhance Raman scattering (SERS)[4].

In order to serve as effective sensors in solution, it is ideal to prepare 2D plasmonic NP arrays in bulk that are readily solvated, thereby creating a high surface area sensor that enhances the rate of analyte-sensor interaction. Several previous studies have focused on preparing 2D plasmonic NP arrays on solid substrates[2,5–7]. However, these fabrication methods do not allow for the transfer of the array from the solid support to solution. Immobile sensors based on solid-supported plasmonic NP arrays suffer in that the surface areas are relatively small, and they rely on the diffusion of the analyte from solution to the array surface for detection to occur. More recently, studies have focused on the synthesis of free-standing plasmonic NP arrays[8–14], which show great promise for producing new materials that are not restricted by the presence of a solid support. While many strategies exist to produce free-standing arrays with large surface areas, very few discuss synthesis methods that result in the formation of arrays that are stable when solvated[11].

In this work, we describe a new synthesis method to prepare water-solvated 2D gold NP (AuNP) arrays that have potential uses as SERS sensors. Our method relies on using peptoid monolayers at the liquid-liquid interface as templates for the assembly of hydrophobically functionalized AuNPs. Peptoids are a relatively new class of sequence-defined polymers that can be precisely engineered to assemble into a variety of structures[15]. In particular, previous work has shown that several amphiphilic peptoid sequences with alternating hydrophobic and ionic monomers are capable of forming nanosheets via the collapse of solid-like monolayers at the air-water[16,17] and liquid-liquid[18] interface. Through this collapse mechanism, the hydrophobic groups of the peptoid are sequestered to the nanosheet interior, while the hydrophilic groups are surface-exposed.

The assembly and collapse of peptoid monolayers at the liquid-liquid interface provides a portal for incorporating hydrophobic species into the nanosheet interior. In our strategy, we use a water-soluble amphiphilic peptoid sequence[16] (Fig. 1A) that is capable of forming a solid-like monolayer at the toluene-water interface. The aliphatic hydrophobic groups of this peptoid monolayer can interact with the aliphatic dodecanethiol ligands of 5.2 nm AuNPs dispersed in toluene (Fig. 1B), forming a composite layer at the toluene-water interface. What makes this method effective at forming solvated 2D AuNP arrays is the ability for the composite layer to collapse at the toluene-water interface, which results in the formation of AuNP-embedded bilayer nanosheets that freely-float in water. Compared to the peptoid sequence traditionally used in nanosheet synthesis[18], the amphiphilic peptoid

[a] Union College, 807 Union St., Schenectady, New York 12308, United States.
†Authors contributed equally to this work.
Electronic Supplementary Information (ESI) available: Procedures for nanosheet synthesis and characterization (UV-vis spectroscopy, optical microscopy, SEM, and AFM); Peptoid sequence studies; Nanosheet image library; Procedure for interfacial tension measurements and Langmuir trough experiments; AFM analysis of AuNPs; EDAX data for the AuNP-embedded nanosheets. See DOI: 10.1039/x0xx00000x

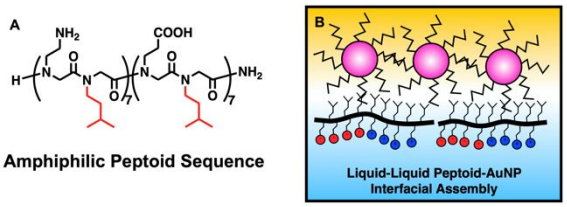

Figure 1. (A) Chemical structure of the amphiphilic peptoid used in the formation of the AuNP-embedded nanosheets. The hydrophobic groups that can interact with the hydrophobically-functionalized AuNPs at the toluene-water interface are highlighted in red. (B) Cartoon depicting the peptoid monolayer as a template for the assembly of dodecanethiol-functionalized AuNPs at the toluene-water interface.

sequence reported here is particularly effective at producing AuNP-embedded nanosheets (see the SI).

To form the AuNP-embedded nanosheets, we prepared a vial containing a 20 µM solution of the peptoid in 10 mM Tris buffer (pH 8). On top of the aqueous phase, we gently dispensed a 2 µM solution of the the 5.2 nm dodecanethiol-functionalized AuNPs in toluene. Agitating the vial induced the collapse of the composite interfacial layer and partitioning of the resulting bilayer material to the aqueous phase. The fabrication of these solvated 2D AuNP arrays was readily observed by eye based on the optical properties of the AuNPs (Fig. 2). AuNPs have well-defined LSPR peaks that appear between 400 and 500 nm, thus giving AuNP solutions their pink to purple colour[19]. As we agitated the vials, we observed elastic-like pink films descending into the aqueous phase, followed by the appearance of pink sheets in solution (Fig. 2A). The solvation of the AuNP-embedded nanosheets is likely due to the hydrophilic

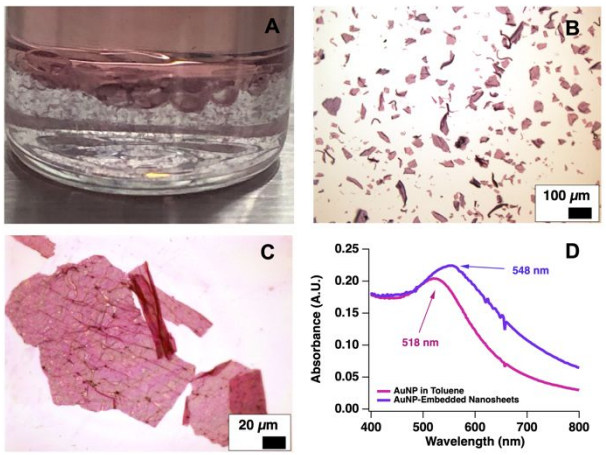

groups of the peptoid that are exposed on the nanosheet surfaces.

Figure 2. (A) A vial containing a 20 µM solution of peptoid in the aqueous phase and 2 µM of AuNP in the toluene phase after agitation. Pink AuNP-embedded nanosheets can be seen in the aqueous phase. (B, C) Optical microscopy images of the AuNP-embedded sheets solvated in the aqueous phase. (D) UV-vis spectra of the AuNP nanoparticles dispersed in toluene (pink trace) and of the AuNP sequestered in the nanosheet (purple trace). The LSPR peak shift from 518 nm to 548 nm when the AuNPs partition from the toluene to the nanosheet interior.

To better visualize the nanosheets, we transferred a drop of the aqueous phase containing the sheets to a thermal silicon oxide wafer and obtained light microscope images of the drop (Fig. 2B and C). The optical microscope images reveal several pink sheet-like structures that are tens of micrometres in lateral dimensions. A variety of shapes with sharp edges can also be seen in a magnified image of the nanosheets (Fig. 2C), indicating an irregular collapse of the peptoid-AuNP composite layer at the interface. Despite this heterogeneity, the sheets overall appear uniform in colour, suggesting that the thickness of AuNPs within the sheets is relatively uniform.

We characterized the plasmonic properties of the AuNP-embedded nanosheets by obtaining UV-vis spectra of the aqueous phase containing the AuNP-embedded nanosheets and comparing it to the UV-vis spectrum of the AuNPs dispersed in toluene (Fig. 2D). When the AuNPs are dispersed in toluene, the LSPR peak appears at 518 ± 2 nm (λ_0), and when the AuNPs are embedded in the nanosheet, the LSPR peak appears at 548 ± 6 nm, corresponding to $\Delta\lambda$ = 30 nm. The AuNP LSPR peak position is highly sensitive to its local environment. An increase in the refractive index of the media surrounding the AuNP results in the LSPR peak shifting to higher wavelengths[1]. The refractive index of toluene is 1.50[20], while the refractive index of water is 1.33 at room temperature[21]. In addition, the refractive indexes of aliphatic species similar to the hydrophobic groups of the peptoid are typically less than 1.50[22]. The red shift of the LSPR peak position is thus consistent with the coupling of the LSPRs on neighbouring AuNPs[2] that results from packing the AuNPs in the nanosheet rather than changing the refractive index of the AuNP environment. We can approximate the interparticle gap distance in the nanosheet based on coupled dipole approximation (CDA) simulations that have been performed on 2D NP arrays with different lattice arrangements[23]. The observed value of $\Delta\lambda/\lambda_0$ (0.0578) is consistent with a gap distance/diameter of 0.649. This value corresponds to a surface-surface interparticle gap distance of 3.4 nm for a hexagonal lattice of 5.2 nm particles, which we expect to be the most likely arrangement for dodecanethiol-functionalized AuNPs in a 2D array[24,25]. This approximate interparticle gap distance is slightly larger than the gap distance of 2.9 nm that has been observed in monolayers of 5.6 nm dodecane-functionalized AuNPs deposited from the air-water interface[24].

To characterize the structural properties of the AuNP-embedded nanosheets, we compared optical microscopy, scanning electron microscopy (SEM), and atomic force microscopy (AFM) images of dry peptoid nanosheets formed at the toluene-water interface in the absence of AuNPs (Fig. 3) to those of the dry AuNP-embedded nanosheets (Fig. 4). These measurements also provide insight into the AuNP-embedded nanosheet assembly mechanism. In the absence of AuNPs, the optical microscopy image of the peptoid nanosheets on a thermal silicon oxide wafer appear as light blue films that are barely visible by eye (Fig. 3A). These images indicate that the nanosheets are very thin. The SEM image (Fig. 3B) also shows that the nanosheet surfaces are highly uniform. The AFM image (Fig. 3C) further confirms that the nanosheets are thin with flat surface morphologies. Very small aggregates (~ 5 nm thick) are observed on the surface of the sheet, which likely form along-

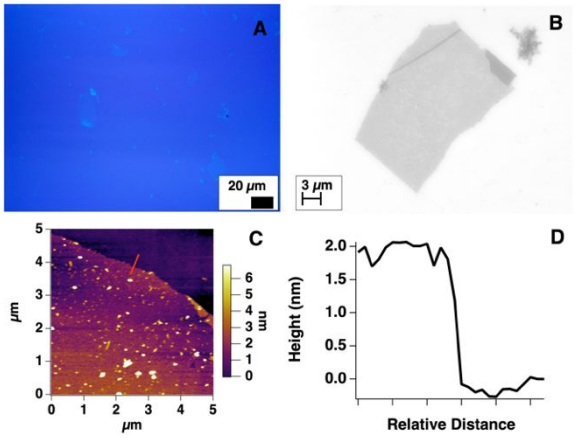

Figure 3. Characterization of peptoid nanosheets formed at the toluene-water interface. (A) Optical microscopy image of dry sheets on a thermal silicon oxide wafer. The sheets appear as flat light blue areas against the dark blue background (B) SEM image of a dry nanosheet. (C) AFM image of a dry nanosheet. The apparent nonuniformity of the sheet surface is due to small aggregates that form during nanosheet synthesis. The red line in the image shows where the line profile was obtained. (D) The line profile shows a nanosheet thickness of ~ 2 nm.

side the nanosheets during monolayer collapse at the toluene-water interface. A representative line profile (Fig. 3D) indicates a nanosheet thickness of ~ 2 nm. The average nanosheet thickness obtained from AFM images of three separate nanosheets is 2.0 ± 0.3 nm, which is consistent with peptoid nanosheets formed from this peptoid at the air-water interface[16].

The structure of the AuNP-embedded nanosheets is quite different than the peptoid nanosheets. The optical microscope image of the AuNP-embedded nanosheet (Fig. 4A) reveals a material that is thicker than the peptoid nanosheets, with surface feature such as wrinkles, folds, and bubbles that appear as yellow areas superimposed over a uniform blue sheet. The SEM image (Fig. 4B) further displays these features as lighter areas in the image. Energy dispersive X-ray mapping of the nanosheets (see the SI) show a greater density of gold in these surface features compared to the flatter areas of the nanosheet, suggesting that the folding of the sheet results in stacking of the AuNPs. These features on the AuNP-embedded nanosheet surface suggest a highly elastic material and likely arise during the compression of the composite layer at the toluene-water interface.

The AFM image of the AuNP-embedded nanosheet (Fig. 4C) further shows that while the sheet is relatively flat, it contains complex surface features that are not present on peptoid nanosheets. A representative line profile of the flat sheet edge (Fig. 4D) shows a thickness of ~17 nm. The average thickness of the uniform region of the AuNP-embedded nanosheets obtained from AFM images of five separate sheets is 17 ± 2 nm. AFM images were also taken of a single layer of AuNPs deposited onto a solid substrate from the air-water interface (see the SI), revealing a thickness of 6.9 ± 0.4 nm. Based on these measurements, the thickness of the AuNP-embedded nanosheet is consistent with a peptoid bilayer and two layers of AuNPs. These AFM measurements indicate that the likely

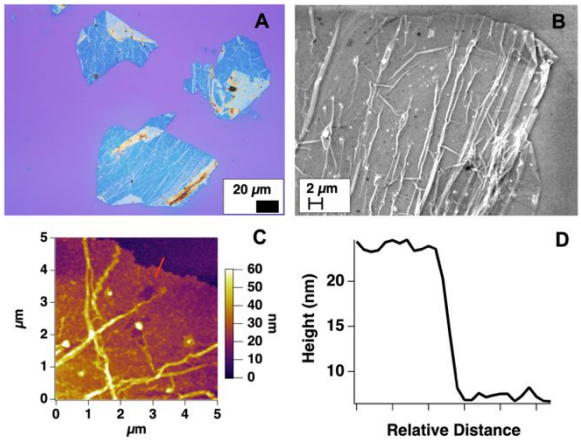

Figure 4. (A) Optical microscopy, (B) SEM, and (C) AFM images of dry AuNP-embedded nanosheets. The red line in the AFM images shows where the line profile was obtained. (D) The line profile shows a sheet thickness of ~17 nm.

formation mechanism is one in which two AuNPs layers become sandwiched between two peptoid monolayers during the collapse of the composite layer at the toluene-water interface. This mechanism, which results in the sequestration of the hydrophobic AuNPs between two peptoid monolayers, is supported by the partitioning of the nanosheets to the aqueous phase upon collapse.

Further insight into the formation mechanism can be determined by monitoring the co-assembly of the peptoid and the AuNPs at the toluene-water interface using pendant drop tensiometry. Here, we measured the surface pressure of the peptoid adsorbing from the aqueous phase (black trace), of the AuNPs adsorbing from the toluene (pink trace), and of the composite system (purple trace) as a function of time (Fig. 5A). These data show that in all systems, the surface pressure rapidly increases over the first few minutes of interface formation, and then no longer changes significantly after 5 minutes. Thus, assembly of the peptoid monolayer, the AuNP monolayer, and the composite layer at the toluene-water interface is relatively fast.

Surface pressure measurements also reveal the relative interactions between the different components assembled at a fluid interface[26,27]. Here, the extent to which the surface pressure of the composite layer is different than either the peptoid or AuNP monolayer gives an indication as to the extent

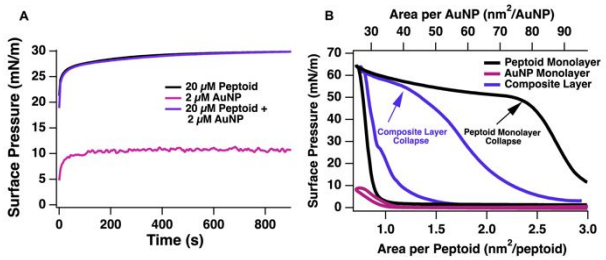

Figure 5. (A) Surface pressure measurements of the toluene-water interface as a function of time when 20 μM peptoid is dissolved in the aqueous phase (black trace), when 2 μM AuNP is dispersed in the toluene phase (pink trace), and when both peptoid are AuNP are present (purple trace). (B) Surface pressure vs. surface area isotherms for the peptoid monolayer (black trace), the AuNP monolayer (pink trace) and composite layer (purple trace) performed in a Langmuir trough at the air-water interface. The arrows indicate the collapse points for the peptoid monolayer and composite layer.

of interactions between the peptoid and AuNPs in the composite layer. While the surface pressure of the mixed system (30.4 ± 0.1 mN/M) is greater than the surface pressure of the AuNP monolayer (10.7 ± 0.4 mN/m), it is not significantly different than that of the peptoid monolayer (29.9 ± 0.9 mN/m). In fact, the data for the peptoid monolayer are nearly indistinguishable from the data for the composite layer. These results suggest that the peptoid monolayer drives the assembly of the composite layer and that the extent of the AuNP ligand-peptoid interactions are similar to the peptoid-peptoid interchain interactions.

We also measured the surface pressure vs. surface area of the peptoid monolayer (black trace), the AuNP monolayer (pink trace), and the composite layer (purple trace) in a Langmuir trough (Fig. 5B). Although these studies were performed at the air-water interface, they provide insight into the effect of AuNPs on the collapse of the peptoid monolayer. The collapse of the peptoid monolayer (black arrow) occurs at an area of 2.3 ± 0.1 nm^2 per peptoid. Significant hysteresis of the isotherm indicates the removal of material from the surface[17]. In the absence of peptoid, the lack of significant hysteresis in the AuNP isotherm suggests that the monolayer does not collapse into the aqueous phase like the peptoid monolayer does. Collapse of the composite layer (purple arrow) occurs at an area of 1.4 ± 0.2 nm^2 per peptoid and an approximate interparticle gap distance of 2 nm. Significant hysteresis indicates the removal of material from the surface. Thus, the addition of the AuNPs to the peptoid monolayer does not disrupt its ability to form nanosheets but creates a more compressible layer that requires a larger surface area change for collapse to occur. This increase in compressibility is consistent with the folds and wrinkles that appear during monolayer compression in a Langmuir trough (see the SI), and the appearance of these features on the surfaces of the AuNP-embedded nanosheets.

In conclusion, we have demonstrated a new synthetic route to produce solution-stable 2D AuNP arrays using peptoid monolayers as templates for assembly at the toluene-water interface. This powerful method allows for the integration of disparate materials from separate phases into a solvated 2D array. The peptoid-AuNP composite layer forms rapidly at the interface and readily collapses to form AuNP-embedded nanosheets in the aqueous phase. Our results are consistent with a 2D structure in which 2 layers of 5.2 nm dodecanethiol-functionalized AuNPs are sequestered between 2 peptoid monolayers. In each AuNP layer, the interparticle gap is approximately 3.5 nm. That the AuNPs are packed in the nanosheets indicates that these materials are promising candidates for SERS sensing. We believe a similar structure would be observed in nanosheets formed with any 5 nm dodecanethiol-functionalized NP, such as those composed of silver. This versatile method for producing solution-stable 2D NP arrays has the potential to be extended to many hydrophobically functionalized NPs that have a range of different optical, electronic, and magnetic properties.

This was supported by funds from Union College, its Chemistry Department, and the Community Foundation for the Greater Capital Region's Bender Scientific Fund. Portions of this work were performed as a User project at the Molecular Foundry, both of which are supported by the Office of Science, Office of Basic Energy Sciences, of the U.S. Department of Energy under contract No. DE-AC02-05CH11231.

Conflicts of interest

There are no conflicts to declare.

Notes and references

1 K. A. Willets and R. P. Van Duyne, *Annu. Rev. Phys. Chem.*, 2007, **58**, 267–297.
2 V. Lotito and T. Zambelli, *Adv. Colloid Interface Sci.*, 2017, **246**, 217–274.
3 B. M. Reinhard, M. Siu, H. Agarwal, A. P. Alivisatos and J. Liphardt, *Nano Lett.*, 2005, **5**, 2246–2252.
4 D.-W. Li, W.-L. Zhai, Y.-T. Li and Y.-T. Long, *Microchim. Acta*, 2014, **181**, 23–43.
5 W. Li, X. Zhao, Z. Yi, A. M. Glushenkov and L. Kong, *Anal. Chim. Acta*, 2017, **984**, 19–41.
6 S. Krishnamoorthy, S. Krishnan, P. Thoniyot and H. Y. Low, *ACS Appl. Mater. Interfaces*, 2011, **3**, 1033–1040.
7 N. Vogel, C. Fernández-López, J. Pérez-Juste, L. M. Liz-Marzán, K. Landfester and C. K. Weiss, *Langmuir*, 2012, **28**, 8985–8993.
8 Q. Cheng, L. Song, H. Lin, Y. Yang, Y. Huang, F. Su and T. Chen, *Langmuir*, 2020, **36**, 250–256.
9 C. Guan, L. Zhang, S. Liu, Y. Wang, W. Huang, C. Zhang and J. Liao, *Langmuir*, 2015, **31**, 3738–3744.
10 J. Lee, G. Bhak, J.-H. Lee, W. Park, M. Lee, D. Lee, N. L. Jeon, D. H. Jeong, K. Char and S. R. Paik, *Angew. Chem. Int. Ed.*, 2015, **54**, 4571–4576.
11 Z. G. Estephan, Z. Qian, D. Lee, J. C. Crocker and S.-J. Park, *Nano Lett.*, 2013, **13**, 4449–4455.
12 T. Andryszewski, M. Iwan, M. Hołdyński and M. Fiałkowski, *Chem. Mater.*, 2016, **28**, 5304–5313.
13 K. C. Ng, I. B. Udagedara, I. D. Rukhlenko, Y. Chen, Y. Tang, M. Premaratne and W. Cheng, *ACS Nano*, 2012, **6**, 925–934.
14 Q. Shi and W. Cheng, *Adv. Funct. Mater.*, 2020, **30**, 1902301.
15 J. Sun and R. N. Zuckermann, *ACS Nano*, 2013, **7**, 4715–4732.
16 E. J. Robertson, E. M. Nehls and R. N. Zuckermann, *Langmuir*, 2016, **32**, 12146–12158.
17 17 B. Sanii, R. Kudirka, A. Cho, N. Venkateswaran, G. K. Olivier, A. M. Olson, H. Tran, R. M. Harada, L. Tan and R. N. Zuckermann, *J. Am. Chem. Soc.*, 2011, **133**, 20808–20815.
18 E. J. Robertson, G. K. Olivier, M. Qian, C. Proulx, R. N. Zuckermann and G. L. Richmond, *Proc. Natl. Acad. Sci.*, 2014, **111**, 13284–13289.
19 S. K. Ghosh and T. Pal, *Chem. Rev.*, 2007, **107**, 4797–4862.
20 M. Debenham and G. D. Dew, *J. Phys. [E]*, 1981, **14**, 544–545.
21 I. Thormählen, J. Straub and U. Grigull, *J. Phys. Chem. Ref. Data*, 1985, **14**, 933–945.
22 A. Aucejo, M. C. Burguet, R. Munoz and J. L. Marques, *J. Chem. Eng. Data*, 1995, **40**, 141–147.
23 X. Ben and H. S. Park, *J. Phys. Chem. C*, 2011, **115**, 15915–15926.
24 V. Santhanam, J. Liu, R. Agarwal and R. P. Andres, *Langmuir*, 2003, **19**, 7881–7887.
25 V. A. Turek, M. P. Cecchini, J. Paget, A. R. Kucernak, A. A. Kornyshev and J. B. Edel, *ACS Nano*, 2012, **6**, 7789–7799.
26 T. F. Moghadam and S. Azizian, *Colloids Surf. Physicochem. Eng. Asp.*, 2014, **457**, 333–339.
27 J. Saien, A. Rezvani Pour and S. Asadabadi, *J. Chem. Eng. Data*, 2014, **59**, 1835–1842.

